Diurnal Variations in Summertime Surface Wind upon Japanese Plains: Hodograph Rotation and Its Dynamics

Takatoshi SAKAZAKI

Department of Earth Sciences, Faculty of Science, Hokkaido University, Sapporo, Japan

and

Masatomo FUJIWARA

Faculty of Environmental Earth Science, Hokkaido University, Sapporo, Japan

(*Manuscript received 25 February 2008, in final form 1 July 2008*)

Abstract

This study investigates diurnal variations in surface wind in Japan during June–August of 1992–2006 using data from the Automated Meteorological Data Acquisition System (AMeDAS) and the Sapporo City Multisensor (MULTI). Harmonic analysis and hodograph analysis are employed to investigate the rotation direction and rotation rate of the wind vector at about 1000 stations. An analysis of six major plains in Japan reveals distinct clockwise and anticlockwise hodograph regions within each plain. The rotation direction is attributed to two lagged pressure-gradient forces of contrasting orientations: one between the land and sea, and another between the plain and adjacent mountains. An analysis of the linearized equations of motion reveals that rotation of the wind vector is mainly controlled by the balance between the pressure gradient force and the frictional force, with a small but non-negligible contribution by the Coriolis force, particularly near the coast. The observed rotation rates of the hodographs show a brief stagnation during the mid-afternoon and a longer stagnation during the nighttime. This irregular rotation rate is well explained by taking into account the semidiurnal component of the wind. The linearized equations of motion indicate that this semidiurnal component results from the semidiurnal component of the pressure gradient force, which is generated by non-sinusoidal solar heating over the course of a day.

1. Introduction

Diurnal variations in surface wind mainly result from local circulations such as land–sea and mountain–valley breezes. In particular, diurnal wind variations upon coastal plains, where most of the global population resides, are an important factor in controlling problems related to pollution and heat-island effects. The land–sea breeze prevails in areas of coastal plains (e.g., see Miller et al. 2003 for a review), controlling the transport of pollutants (e.g., Kurita et al. 1990; Puygrenier et al. 2005). Those parts of plains located close to mountains are also subjected to mountain–valley (or mountain–plain) breezes, which may become coupled with the land–sea breeze to generate a regional-scale wind system (e.g., Kondo 1990). Thus, diurnal variations in wind patterns upon coastal plains commonly involve multiple components, strongly affected by topography. For this reason, most previous observational or numerical studies have focussed on a particular region.

Corresponding author and present affiliation: Takatoshi Sakazaki, Graduate School of Environmental Science, Hokkaido University, Sapporo, Hokkaido 060-0810, Japan
E-mail: zaki@ees.hokudai.ac.jp

The hodograph is the most suitable approach in describing diurnal variations in the wind vector at a given point. In the case that the region of interest is influenced by local-scale circulations, the hodograph rotates over the course of a day. Previous studies have investigated the dynamics that control the shape, direction, and rotation rate of the surface-wind hodograph. Haurwitz (1947) analyzed hodographs in coastal areas and found that they rotate clockwise. The author employed a set of simple linear equations of motion to investigate the hodograph associated with a land–sea breeze, and considered a single pressure gradient force corresponding to that between land and sea. The author concluded that it is the Coriolis force that rotated the hodographs in a clockwise direction.

According to Haurwitz's (1947) theory, the rotation direction should always be clockwise, and the rotation rate should be the same between during the daytime and during the nighttime; however, subsequent observational studies have reported anticlockwise rotation directions (e.g., Mori 1982; Furberg et al. 2002) and different rotation rates from those predicted by Haurwitz (e.g., Neumann 1977; Zhong and Takle 1992; Furberg et al. 2002).

Several theoretical studies have sought to explain the observed anticlockwise rotations and complex rotation rates. Kusuda and Alpert (1983) proposed a simple analytical theory for anticlockwise rotation. The authors considered two different forces in a horizontal plane, and showed that anticlockwise rotation could occur in the case of a phase difference between the forces. The two forces might correspond to a sea breeze system and a larger-scale flow effect (Fisher 1960; Itoh 1983, 1989; Prezerakos 1986; Helmis et al. 1995; Simpson 1996), or a land–sea pressure gradient force and a topographically induced pressure gradient force (Mass 1982; Ookouchi and Wakata 1984; Orlic et al. 1988; Steyn and Kallos 1992; Simpson 1996; Bastin et al. 2005; Nitis et al. 2005).

In terms of rotation rate, Neumann (1977) and Kusuda and Alpert (1983) derived equations for angular velocity of the hodograph that take into account nonlinear (advective) and background-flow effects. Based on these equations, the controlling factors of the rotation rate have been studied using a scale analysis method (Lecluyse and Neumann 1986; Simpson 1996), observation data (Kusuda and Abe 1989), and via numerical simulations (Steyn and Kallos 1992; Zhong and Takle 1993). The results of these studies suggest that the pressure gradient force, the Coriolis force, and the frictional force are of near-equal importance, with occasional, local effects of the advective term. It should be noted that most previous observational studies used data from less than 50 stations. Because the hodograph at a given station can be strongly affected by the local topography, it is likely that more than 50 stations are required to obtain robust conclusions. In addition, most observational and numerical studies focus on a particular region, and it is commonly unclear whether the results can be applied to other regions.

A dense surface-weather observation network, termed the Automated Meteorological Data Acquisition System (AMeDAS), has been established in Japan. The network consists of about 920 stations that monitor wind and other meteorological parameters at a horizontal interval of ~21 km. In addition, a much denser surface-weather network comprising 52 stations (horizontal interval of ~5 km) has been established upon the Ishikari Plain, Hokkaido, northern Japan.

Using these data sets, we investigate the statistical characteristics of the surface-wind hodograph mainly for six major plains (each at least 100 km across) in Japan. We demonstrate that the hodograph rotation direction for these areas can be explained by a combined land–sea and mountain–plain breeze system, and that diurnal variations in the rotation rate can be attributed to non-sinusoidal solar heating over the course of a day.

The remainder of the manuscript is organized as follows. Section 2 describes the geographical features of the study areas, data sets, and analysis methods, while Section 3 describes the statistical characteristics of the surface wind hodographs for the analyzed Japanese plains. In Section 4, we investigate the controlling factors of hodograph rotation direction and rate, based on linearized equations of motion. Finally, the main findings of the study are summarized in Section 5.

2. Data and Analysis Methods

The AMeDAS network is operated by the Japan Meteorological Agency, and monitors horizontal wind direction and speed, temperature, precipitation amount, and sunshine duration throughout Japan. Measurements were taken every 10 minutes during 1994–2006, and every hour during earlier years. In this paper, we use 10-minute averages of wind velocity for each hour (e.g., the average of measurments from 5:50 to 6:00 is used for the data

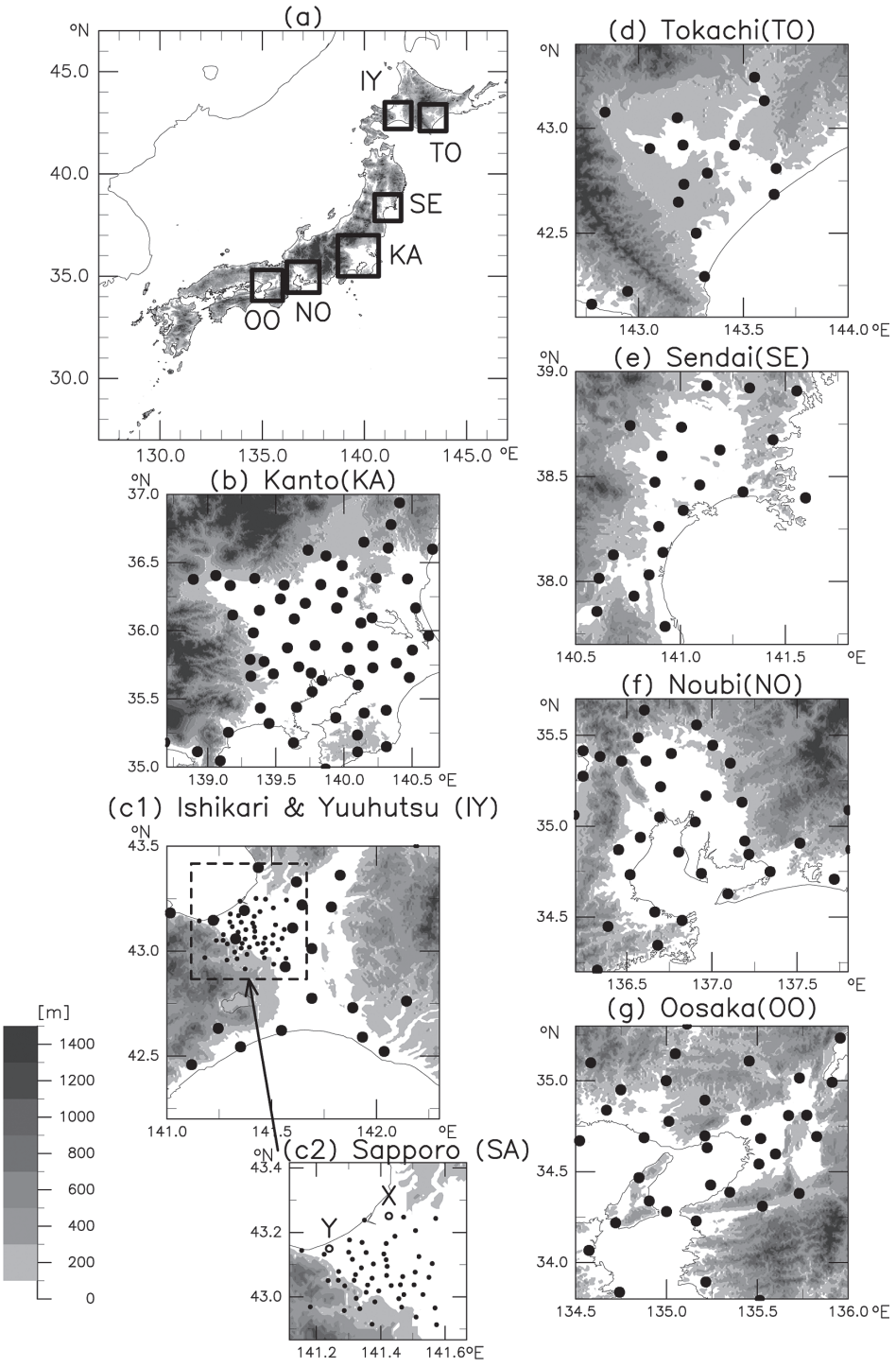

Fig. 1. (a) Map of Japan showing the locations of the six selected study regions. No topographic information is shown on the Asian continent. Station locations and detailed topography are shown for (b) Kanto (KA), (c1) Isikari and Yuuhutsu (IY), (d) Tokachi (TO), (e) Sendai (SE), (f) Noubi (NO), and (g) Oosaka (OO). In the IY region (c1), the Sapporo (SA) region (c2) is represented by a dashed square. Large solid circles denote AMeDAS stations, while small solid circles in the SA region (c2) represent MULTI stations. Wind data at X and Y (open circles in c2) are shown in Fig. 2. At this latitude, 1° of longitude corresponds to ~90 km.

at 6:00) for the period June–July–August (JJA) of 1992–2006, the season when local circulations (e.g., land–sea breezes) prevail. Of the 920 AMeDAS stations, we focus on those located at altitudes below 200 m (699 stations in total), especially those located upon the six major plains of interest. We also consider data collected by the dense Sapporo City Multisensor (MULTI) network deployed upon Ishikari Plain, Hokkaido (Fig. 1c2, SA region), which has an average horizontal spacing of ~5 km and temporal resolution of 10 minutes. For this network, we used 10-minute averages of wind velocity at every hour, for the same period as that for the AMeDAS data.

Figure 1 shows the locations of the six regions selected for analysis: Kanto (KA), Ishikari and Yuuhutsu (IY) including Sapporo (SA), Tokachi (TO), Sendai (SE), Noubi (NO), and Oosaka (OO). All of these regions contain plains that face the sea along about 25% of the region boundary; the plains are surrounded by mountains that define the other 75% of the region boundary. The horizontal scale is ~100 km for KA, ~50–100 km for the other five plains, and ~30 km for SA (Fig. 1c2). We note that Japanese Standard Time (JST) is defined at (35° N, 135°E) and that the AMeDAS network ranges between ~130°E and ~145°E. Although the local standard time varies among the stations with longitude, we neglect these differences (of up to 1 hour) in this study.

The procedures employed in data processing and analysis are as follows. First, by averaging the data for JJA of 1992–2006, mean summertime hourly data are calculated for each station. Using this data set, the anomaly wind (u for the eastward component; v for the northward component) is extracted from the 24-hour mean.

The left-hand panels in Fig. 2 show two typical examples of hodographs constructed from hourly anomaly vectors (u, v), for stations X and Y shown in Fig. 1c2. Note that the hodograph rotates anticlockwise at X, yet clockwise at Y. In addition, the nighttime data points define a tighter cluster than the daytime points.

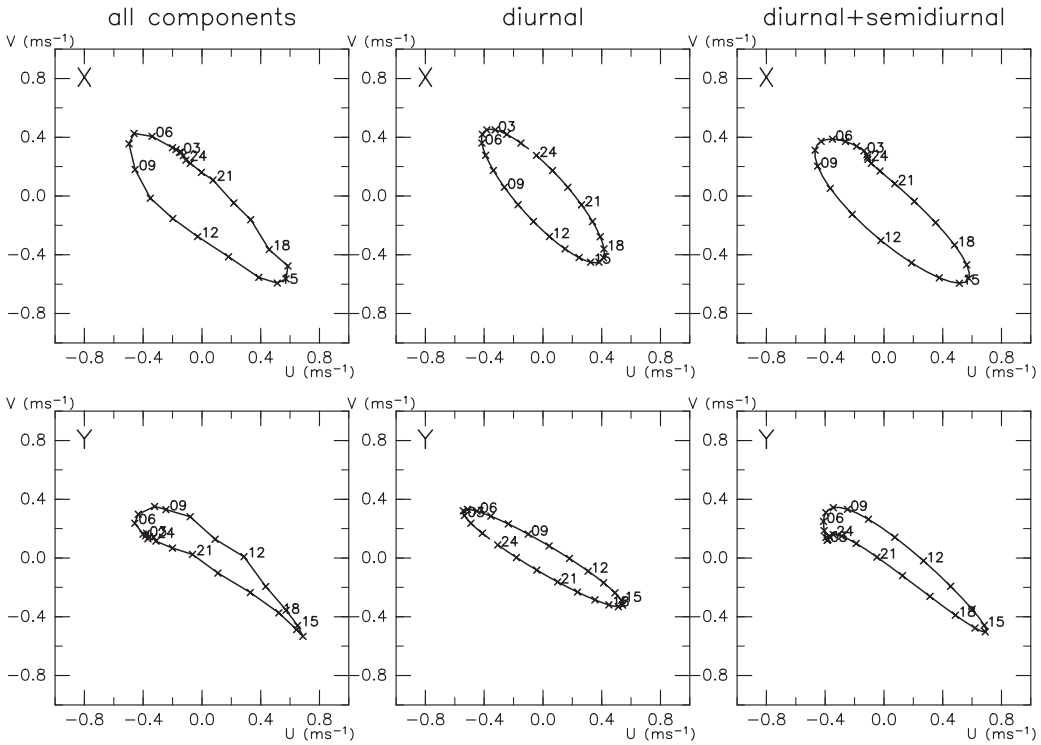

Fig. 2. Hodograhs at stations X (top) and Y (bottom) shown in Fig. 1c2. (left) Hodographs of hourly anomaly wind. (center) Hodographs reconstructed using the diurnal component only. (right) Hodographs reconstructed using the diurnal and semidiurnal components. The numbers represent Japanese Standard Time (JST).

Next, u and v are decomposed into 11 sinusoidal functions by harmonic analysis:

$$u = \sum_{m=1}^{11} u_m \sin(m\omega t + \alpha_m) \quad (1)$$

$$v = \sum_{m=1}^{11} v_m \sin(m\omega t + \beta_m) \quad (2)$$

where ω is the angular velocity of the Earth's rotation, and (u_m, v_m) and (α_m, β_m) are the amplitudes and phase shifts for the m-th component, respectively. Note that $0 < \alpha_m, \beta_m < 2\pi$. The least squares method is used for the actual calculation.

Table 1 shows the relative amplitudes of the harmonic components normalized by the diurnal (m = 1) component. These amplitudes are the averages for those AMeDAS stations located at altitudes below 200 m (699 in total). For both eastward and northward components, the amplitude of the diurnal component is nearly three times larger than that of the semidiurnal component, the second largest. This finding confirms the validity of using only the diurnal component as the first approximation, as employed in previous works (e.g., Alpert et al. 1984; Gille et al. 2005).

Following Kusuda and Abe (1989), the rotation direction of the hodograph is defined as

$$\sin(\alpha_1 - \beta_1) < 0 \text{ for clockwise,} \quad (3)$$

$$\sin(\alpha_1 - \beta_1) > 0 \text{ for anticlockwise.} \quad (4)$$

Here, the rotation direction is defined using only the diurnal component, because of its dominance. The center panels in Fig. 2 show the hodographs reconstructed from the diurnal component only, whereas the right-hand panels show the hodographs reconstructed from the diurnal and semidiurnal components. The former hodographs represent the general features of the original hodographs reasonably well (i.e., the shape and rotation direction), while the latter show the detailed irregular wind-vector rotation of the original hodographs.

We also compute the rotary spectra (i.e., clockwise and anticlockwise spectra) to assess the statistical significance of the rotation direction defined above (e.g., Orlic et al. 1988; see Gonella 1972 for details on rotary spectral analysis). The two rotary spectra at each station are computed using the JJA 3-month continuous data set for each year, and are averaged for 11 years for most stations. A 3-point running average is then applied in the frequency domain.

The significance of the spectral peaks is assessed using the χ^2 distribution with k degrees of freedom. In the present case, $k = 4 \times 3 \times M$, where the factor 4 is the number of variables (u_m, v_m, α_m, β_m in Eqs. (1) and (2)) used to represent the rotary spectra, the factor 3 is the number of points used for the running average, and M is the number of data sets (i.e., the number of years averaged). The total spectrum (summation of clockwise and anticlockwise spectra) represents the mean kinetic energy. The difference between the two spectra indicates the rotation direction.

Figure 3 shows the results of rotary spectral analysis for stations X and Y. We observe significant diurnal and semidiurnal peaks in the total spectrum. The rotary spectrum difference shows that at X (Y), the diurnal peak of the anticlockwise (clockwise) spectra is significantly greater than that of the clockwise (anticlockwise) spectra. These findings are consistent with the results of the hodograph analysis shown in Fig. 2. The rotary spectrum difference of the diurnal peak is used to confirm the validity of the rotation direction defined by Eqs. (3) and (4). That is, the rotation direction is only specified when the two estimations are in agreement. Of the 699 stations located at altitudes below 200 m, we obtained a statistically significant rotation direction for 506.

To describe the rotation rate of each hodograph, three quantities are calculated every hour. Let $\boldsymbol{V}_i$ (i = 1, 2, ..., 24) be the hourly anomaly surface-wind vector (u, v) at i JST. The first quantity is the angle between $\boldsymbol{V}_i$ and $\boldsymbol{V}_{i-1}$, which has been commonly used in previous studies (e.g., Neumann 1977; Kusuda and Alpert 1983). The second quantity is the difference in wind speed between $\boldsymbol{V}_i$ and $\boldsymbol{V}_{i-1}$ (i.e., $\| \mathbf{V}_i | - | \mathbf{V}_{i-1} \|$, and the third quantity is the magnitude of the displacement vector (i.e., $|\mathbf{V}_i - \mathbf{V}_{i-1}|$).

3. Results

Figure 4 shows the hodograph of the hourly anomaly surface wind (u, v) obtained using MULTI data for the SA region (Fig. 1c2). Figure 4a represents all components, 4b only the diurnal component, and 4c the diurnal and semidiurnal components. The hodographs in Fig. 4b largely represent the shape of the original hodographs shown in Fig. 4a, and the hodographs in Fig. 4c represent the detailed shape of the original hodographs. In the following sections, we examine the statistical char-

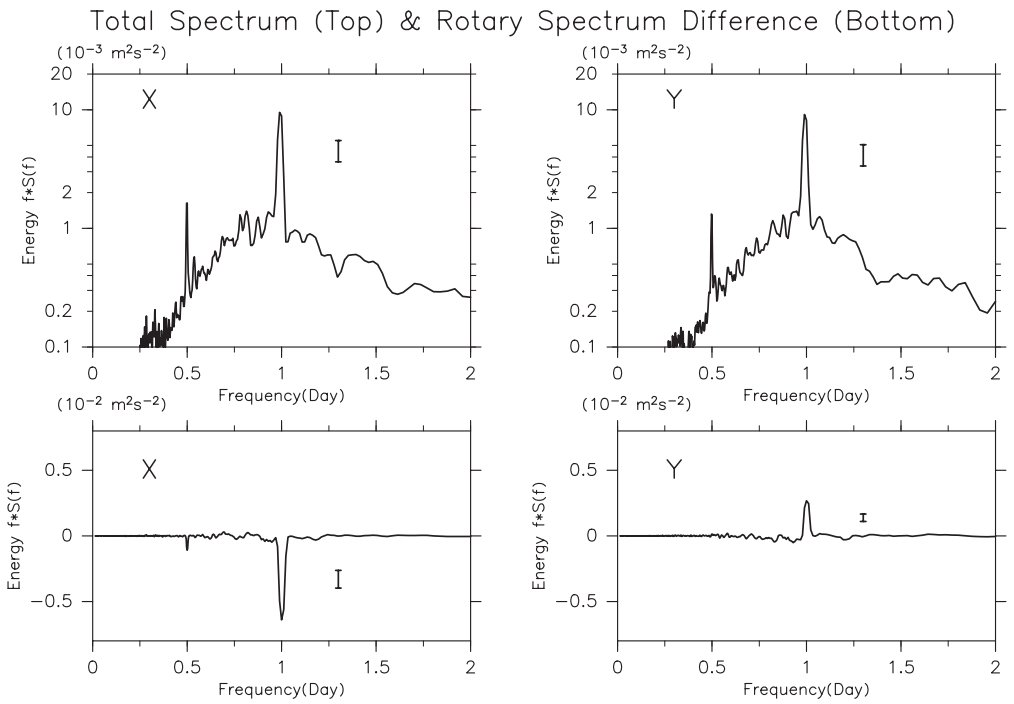

Fig. 3. (top) Total spectrum (clockwise plus anticlockwise spectra) and (bottom) the difference between the two spectra (clockwise minus anticlockwise). Left (right) panels are for stations X (Y) in Fig. 1c2. The 95% confidence interval is shown in each panel. The intervals in the top panels are for all peaks because the spectrum is plotted on a semi-log scale. The intervals in the bottom panels are only for the diurnal peak because the spectrum is plotted on a linear–linear scale.

acteristics of the rotation direction (Section 3.1) and rotation rate (Section 3.2) of the surface-wind hodograph.

3.1 Rotation direction

Figures 4b and 4c clearly show that the hodographs with a clockwise (anticlockwise) rotation are found mostly in the north-eastern (south-western) part of the Ishikari Plain, where the mountains are located to the right (left) when facing the sea. The major axes of the ellipses in the central part of the plain are generally oriented normal to the coastline and parallel to the mountain–plain boundary. These observations suggest that diurnal variations in wind upon the Ishikari Plain (except for the region located near the mountains) are mainly controlled by the land–sea breeze, modulated by topographic effects.

Figure 5 shows a time series of surface-wind vectors for the SA region. The station data are interpolated to an 18 × 18 grid (~3.5 km horizontal spacing) using the objective analysis proposed by Barnes (1964) (see also Kurishnamurti and Bounoua 1996). At 00 and 03 JST, the winds upon the plain are generally from the southeast, representing a land breeze. The winds near the mountain regions, upon the northeasternmost and southwesternmost parts of the plain, involve a component blowing from the mountains down to the plain, representing a mountain breeze. The land breeze has strengthened by 06 JST, reaching its maximum value, whereas the mountain breeze shows little change. At 09 JST, the land breeze continues to prevail, but at areas close to the mountains the wind is now blowing from the plain to the mountains, representing the development of a valley breeze. The land breeze upon the plain has weakened by 12 JST, and the winds along the coast have turned onshore, representing a sea breeze. At 15 JST, the sea breeze and the valley breeze are dominant over the region. The sea breeze continues to dominate at 18 JST, but the valley breeze has weakened. Finally, at 21 JST the sea breeze has decayed and the land breeze has started to blow; the

mountain breeze is already strong. The key aspect of these data is that the times when the land, valley, sea, and mountain breezes attain their maxima are lagged one another. We propose that the time lags of these breezes explain the clockwise and anticlockwise rotations of the hodographs for this region. A similar time lag in land–sea and mountain–valley breezes has also been reported from a numerical study of the KA region (Fig. 1b; Kondo 1990).

We now consider the spatial distribution of clockwise and anticlockwise hodographs for other major plains throughout Japan. Figure 6 shows the hodographs of the diurnal component for the six major plains of interest. The figure shows AMeDAS data for stations located at altitudes below 200 m. Clockwise and anticlockwise hodographs occupy distinct regions within each plain, as also observed for the SA region (Fig. 4b). This pattern is most pronounced for KA (Fig. 6a), where clockwise (anticlockwise) hodographs occur in the west (northeast), and the mountains are located to the right (left) when facing the sea. For IY (Fig. 6b), two sets of regions of clockwise and anticlockwise rotation are observed: one upon the Ishikari Plain, which includes the SA region, and another in and around the Yuuhutsu Plain, facing the sea to the south, where clockwise and anticlockwise hodographs occur in the western and eastern coastal regions, respectively. For the region TO (Fig. 6c), the plain of interest faces the sea along the coast between (42.2°N, 143.3°E) and (43.0°N, 144.0°E). Clockwise hodographs are observed in the southwestern part of the plain, with anticlockwise hodographs in the northeastern part. The plain of interest at SE (Fig. 6d) faces the sea along the coast between (37.7°N, 141.0°E) and (38.4°N, 141.5°E). Clockwise hodographs are seen in the southwestern part of the plain, and anticlockwise hodographs in

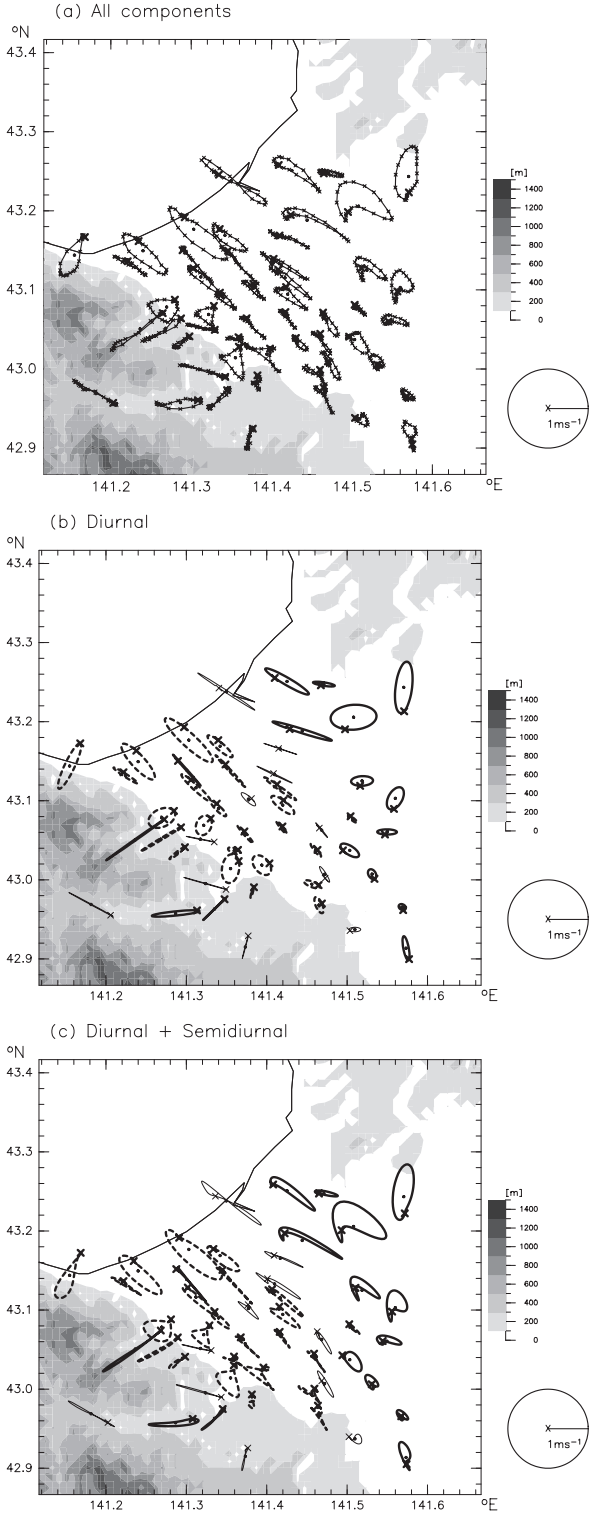

Fig. 4. (a) Hodographs of surface hourly anomaly wind (u, v) derived from MULTI data in the SA region. Gray tones show topography. The symbol X in each hodograph denotes the head point of the wind vector at 00 Japanese Standard Time (JST). (b) Hodographs reconstructed from the diurnal component only. Thick solid and dashed ellipses represent clockwise and anticlockwise rotations, respectively. Thin solid ellipses indicate hodographs for which the direction of rotation is not specified. (c) As for (b), but for hodographs reconstructed from the diurnal and semidiurnal components.

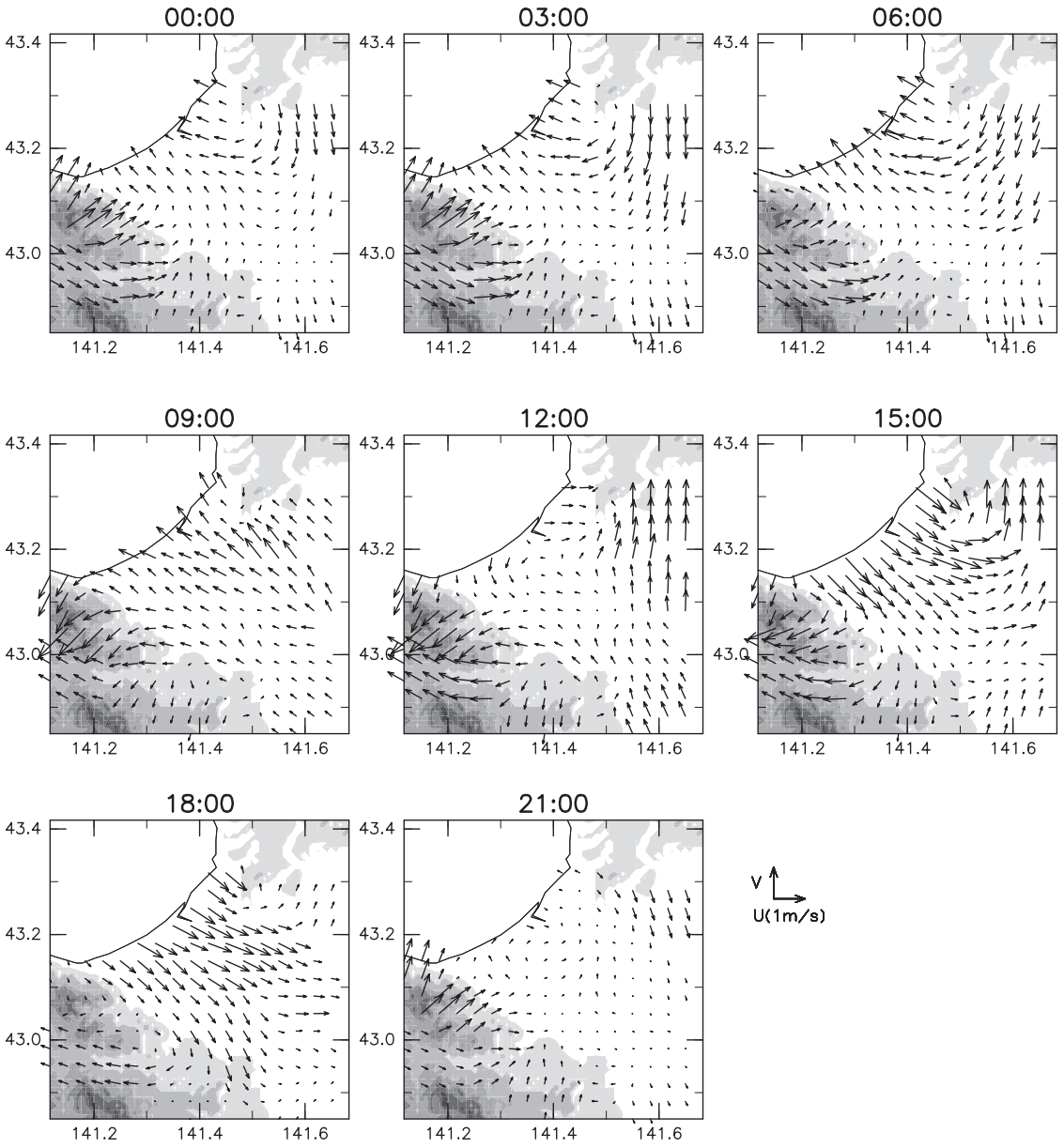

Fig. 5. Time series of the surface-wind vector field in the SA region from 00 JST to 21 JST at 3-hour intervals. Station data were interpolated to an 18 × 18 grid by objective analysis. See text for details.

the northeastern part. The topography of regions NO and OO is relatively complicated, but the two regions record similar distributions of clockwise and anticlockwise rotation directions upon the plains surrounding the respective bays. In region NO (Fig. 6e), clockwise hodographs are seen to the west of the bay, with anticlockwise hodographs to the east. In region OO (Fig. 6f), clockwise hodographs are seen to the north of the bay, and anticlockwise hodographs to the south.

In summary, our analysis of six major plains within Japan reveals that clockwise (anticlockwise) hodographs occur in the regions for which the nearest mountains are located to the right (left) when facing the sea. This distribution is dominantly controlled by the configuration of the plain; namely, the spatial relationship between the coastline and surrounding mountains. In a similar study

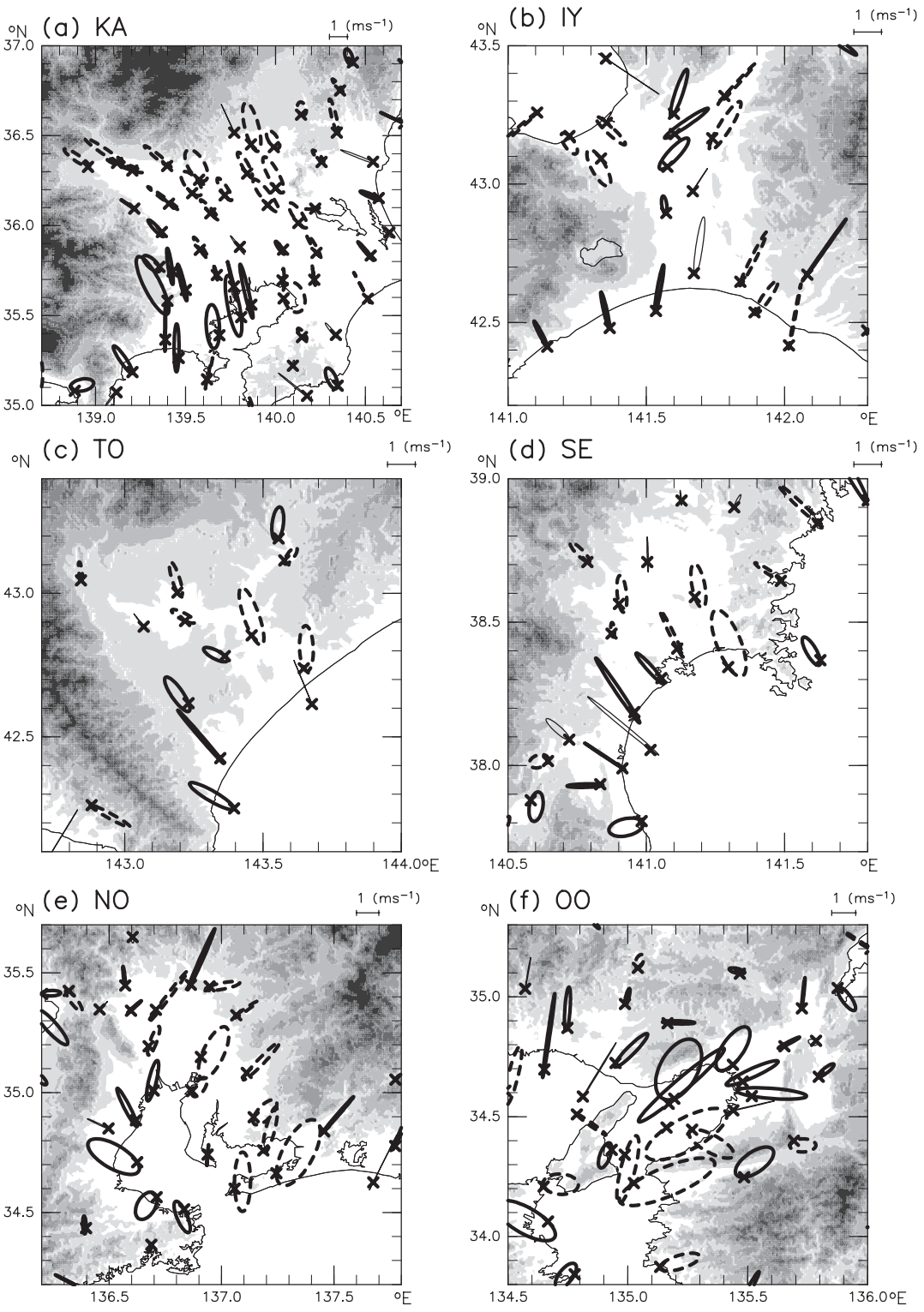

Fig. 6. Hodographs reconstructed from the diurnal component for (a) KA, (b) IY, (c) TO, (d) SE, (e) NO, and (f) OO. Thick solid and dashed ellipses represent clockwise and anticlockwise rotations, respectively. Thin solid ellipses indicate hodographs for which the direction of rotation is not specified.

of surface-wind data for Puget Sound in western Washington State, USA, Mass (1982) reported that clockwise hodographs are distributed on the orographic right slope (i.e., slope located to the right when looking down the valley), while anticlockwise hodographs are distributed on the left. We found a similar distribution pattern for major plains within Japan. Kusuda and Abe (1989) showed a similar spatial partitioning of hodographs in their analyses of Ooita City in Japan and California State in the USA (their Fig. 3), although they did not focus on this aspect of the data in their discussion. We also discussed the possibility that the distribution of clockwise and anticlockwise hodographs may reflect the lagged combination of the land–sea breeze and mountain–valley breeze, with it being unnecessary to invoke the effects of the Coriolis force, even when explaining clockwise hodographs.

We calculated the ratio of the number of stations with anticlockwise hodographs to the total number of stations, which is a key factor in estimating the contribution of the Coriolis force to the rotation direction. In this analysis, we considered AMeDAS stations from all over Japan whose rotation directions were statistically significant and whose altitudes were less than a given critical value. For a critical altitude of 200 m (50 m), the number of anticlockwise stations is 198 (114) and the total number of stations is 506 (320), yielding a ratio of 0.39 (0.36). As these ratios are significantly less than 0.5, it is likely that the Coriolis force has a non-negligible effect on the system. The contribution of the Coriolis force to the rotation direction is discussed in detail in Section 4.1.

3.2 Rotation rate

With regard to the rotation rates of the hodographs, Figs. 2 (left) and 4a show that midnight points (near the X symbols) and some mid-afternoon points tend to stagnate, with the former defining a tighter cluster than the latter. This finding demonstrates that the rotation rate changes over the course of a day, as reported in previous studies (e.g., Staley 1957; Furberg et al. 2002). By definition, such an asymmetric rotation rate cannot be explained solely in terms of the diurnal component. Figures 2 and 4 show that by adding the semidiurnal component, the original hodographs are well represented.

To statistically confirm the role of the semidiurnal component in the rotation rate, the three quantities introduced in the last paragraph of Section 2 are calculated and averaged for AMeDAS stations located at altitudes below 200 m. Figure 7 shows the time series of (a) the angle of two consecutive wind vectors and (b) the change in wind speed over the course of a day. For both quantities, the rotation is slow during the mid-afternoon and nighttime; these features are well reproduced by the diurnal and semidiurnal components. In terms of angle, which is commonly used in characterizing

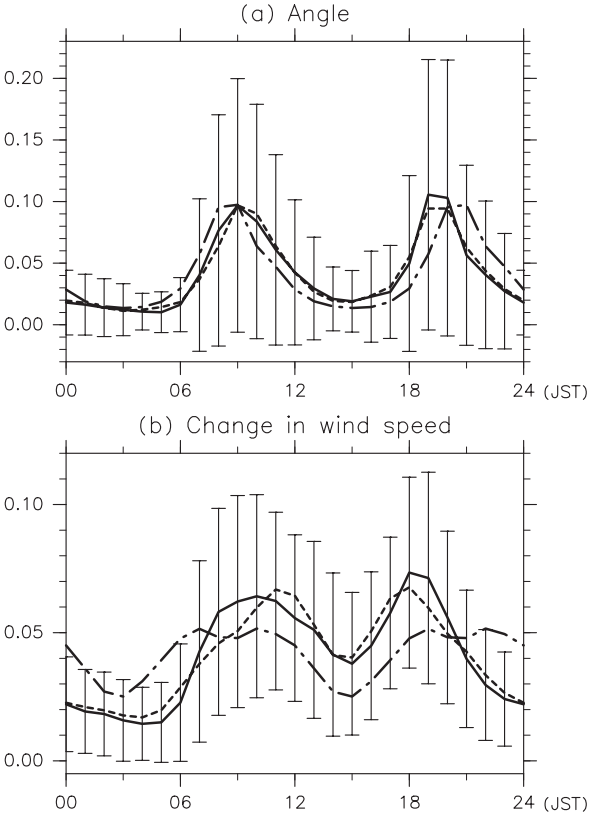

Fig. 7. Time series of rotation rate of the hodograph averaged for those AMeDAS stations located at altitudes below 200 m. (a) Angle between consecutive wind vectors, $\boldsymbol{V}_i$ and $\boldsymbol{V}_{i-1}$. (b) Change in wind speed for consecutive wind vectors, $\|\mathbf{V}_i|-|\mathbf{V}_{i-1}\|$. Values are normalized by the total change over the course of a day. Solid curves with vertical bars represent the original hodograph; the bars represent one standard deviation. Dot-dash curves represent the hodograph reconstructed from the diurnal component only, and dotted curves represent the hodograph reconstructed from the diurnal and semidiurnal components.

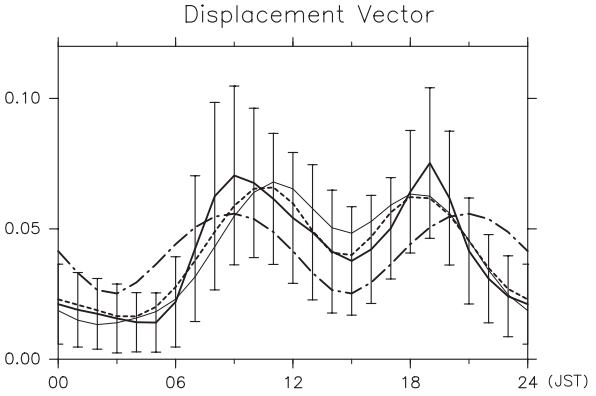

Fig. 8. As for Fig. 7, but for the magnitude of the hourly displacement vector, $|\boldsymbol{V}_i - \boldsymbol{V}_{i-1}|$. Thin solid curve represents the modeled hodograph discussed in Section 4.2.

the rotation rate, the difference between the diurnal curve and the diurnal-plus-semidiurnal curve is insignificant. In contrast, a marked difference between the diurnal curve and the diurnal-plus-semidiurnal curve is observed for the change in wind speed; the semidiurnal component plays an important role in reproducing the observation.

A physically more reasonable way to describe the rotation rate would be to use the displacement vector, which is related to both the angle and the change in wind speed. Figure 8 shows the time series of the magnitude of the displacement vector. The rotation rate shows a brief stagnation during the mid-afternoon and a longer stagnation at night; this asymmetry cannot be explained solely in terms of the diurnal component. The addition of the semidiurnal component, however, enables the observation to be reasonably well explained.

In summary, the semidiurnal component generates the observed asymmetry in the rotation rate over the course of a day. The semidiurnal component also makes a small but significant contribution (approximately 35% of the contribution of the diurnal component) to the diurnal wind variation (Table 1). Furthermore, spectral analysis detects a semidiurnal peak at most stations (e.g., Fig. 3). The origin of the semidiurnal component is further investigated in Section 4.2.

Table 1. Relative amplitudes of the harmonic components of the hourly anomaly wind, as averaged for the 699 AMeDAS stations located at altitudes below 200 m.

	diurnal (m = 1)	semidiurnal (m = 2)	terdiurnal (m = 3)	higher (m > 4)
u_m	1.	0.36	0.12	< 0.07
v_m	1.	0.33	0.11	< 0.06

4. Discussion

In this section, linearized equations of motion are used in describing the hodographs. Nonlinear (advective) terms are assumed to be small for the averaged hodographs treated here, although they may affect individual hodographs. We start with the following momentum equations:

$$\frac{\partial u}{\partial t} - fv + ku = -H_1(t), \tag{5}$$

$$\frac{\partial v}{\partial t} + fu + kv = -H_2(t), \tag{6}$$

where $f = 2\omega \sin\phi$ is the Coriolis parameter, ω is the angular velocity of the Earth's rotation, ϕ is latitude, k is the Rayleigh friction coefficient, and $H_1(t)$ and $H_2(t)$ are the pressure gradient forces.

The pressure gradient forces associated with local circulation are much greater during the daytime than during the nighttime because the forces mainly result from differences in solar heating for different surface conditions (e.g., Cokelet 1992; Zhong and Takle 1992). Following Haurwitz (1947) and Kusuda and Alpert (1983), we assume hat-like functions for $H_1(t)$ and $H_2(t)$, similar to the solar heating function (see Fig. 9):

$$H_1(t) = \begin{cases} A\cos(\omega t - \alpha) & \left(-\frac{\pi}{2} < \omega t - \alpha < \frac{\pi}{2}\right) \\ 0 & \left(-\pi < \omega t - \alpha < -\frac{\pi}{2},\ \frac{\pi}{2} < \omega t - \alpha < \pi\right), \end{cases} \tag{7}$$

$$H_2(t) = \begin{cases} B\cos(\omega t - \alpha - \theta) & \left(-\frac{\pi}{2} < \omega t - \alpha - \theta < \frac{\pi}{2}\right) \\ 0 & \left(-\pi < \omega t - \alpha - \theta < -\frac{\pi}{2},\ \frac{\pi}{2} < \omega t - \alpha - \theta < \pi\right), \end{cases} \tag{8}$$

where t is time (JST), A and B are the coefficients of the forces, α is the phase shift, and θ is the phase difference between $H_1(t)$ and $H_2(t)$. We confine the region of α to $-\pi < \alpha < -\pi/2$, $\pi/2 < \alpha < \pi$ (i.e., 06–18 JST), and the region of θ to $-\pi/2 < \theta < \pi/2$. These regions are based on the assumption

that both $H_1(t)$ and $H_2(t)$ would attain maxima during the daytime (06–18 JST). Thus, A and B can take either positive and negative values, depending on the direction of the forces at their maxima. To obtain an analytical solution for Eqs. (5) and (6), Haurwitz (1947) and Kusuda and Alpert (1983) approximated $H_1(t)$ and $H_2(t)$ by taking only the first two fourier-series terms:

$$G_1(t) = \frac{A}{\pi} + \frac{A}{2}\cos(\omega t - \alpha) \quad (-\pi < \omega t - \alpha < \pi), \tag{9}$$

$$G_2(t) = \frac{B}{\pi} + \frac{B}{2}\cos(\omega t - \alpha - \theta) \quad (-\pi < \omega t - \alpha - \theta < \pi). \tag{10}$$

The second terms of the right-hand sides of Eqs. (9) and (10) correspond to the diurnal component. In Section 4.2, we also consider the second-order component (i.e., the semidiurnal component). The new approximate forms of $H_1(t)$ and $H_2(t)$ are

$$F_1(t) = \frac{A}{\pi} + \frac{A}{2}\cos(\omega t - \alpha) + \frac{2A}{3\pi}\cos(2(\omega t - \alpha)) \quad (-\pi < \omega t - \alpha < \pi), \tag{11}$$

$$F_1(t) = \frac{B}{\pi} + \frac{B}{2}\cos(\omega t - \alpha - \theta) + \frac{2B}{3\pi}\cos(2(\omega t - \alpha - \theta)) \quad (-\pi < \omega t - \alpha - \theta < \pi). \tag{12}$$

Figure 9 also shows the functions $G_1(t)$ and $F_1(t)$, revealing that $F_1(t)$ is a better approximation of $H_1(t)$ than is $G_1(t)$.

4.1 *Contribution of the Coriolis force to the rotation direction*

In Section 3.1, we suggested that two lagged pressure-gradient forces of contrasting orientations (arising from heating differences between the sea and land, and between the mountain and plain) would be essential in determining the distribution of rotation directions. We also found that the number of clockwise hodographs exceeds that of anticlockwise hodographs. This observation suggests a small but non-negligible contribution of the Coriolis force. We now estimate the degree of this contribution based on the linearized equations of motion.

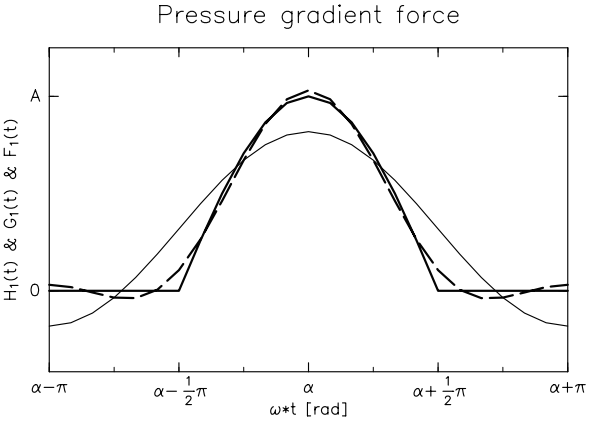

Fig. 9. Modeled pressure gradient force. Here, A is assumed to be positive. The thick solid curve is for $H_1(t)$ in Eq. (7), the thin solid curve is for $G_1(t)$ in Eq. (9), and the thick dashed curve is for $F_1(t)$ in Eq. (11).

Because the rotation direction is defined solely in terms of the diurnal component, the diurnal component of the pressure gradient force (i.e., $G_1(t)$ and $G_2(t)$) is considered here. Note that because of the linearity, the semidiurnal component of the force has no influence on the diurnal component of the wind. We now consider the following equations:

$$\frac{\partial u}{\partial t} - fv + ku = -G_1(t), \tag{13}$$

$$\frac{\partial v}{\partial t} + fu + kv = -G_2(t), \tag{14}$$

where A, B, α, and θ differ for different stations. This set of equations reveals that the system behavior would strongly depend on the magnitude relationship between the Coriolis term and the frictional term, and thus on the magnitude of k. Accordingly, we shall estimate the magnitude of k using AMeDAS observation data in estimating the contribution of the Coriolis force. To this end, we focus on the frequency of (1) the rotation direction of the surface-wind vector, and (2) the rotation direction of the pressure gradient force.

4.1.a *Estimation of k based on the frequency of the rotation direction of the surface-wind vector*

Using Eqs. (13) and (14), Alpert et al. (1984) calculated theoretical anticlockwise frequency dis-

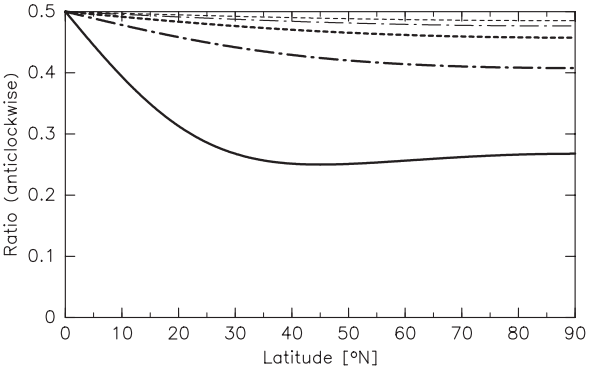

Fig. 10. Theoretical ratio of the number of stations with anticlockwise hodographs to the total number of hodographs. Thick solid curve is for $k = \omega$, thick dot-dash curve is for $k = 2\omega$, thick dotted curve is for $k = 3\omega$, thin dot-dash curve is for $k = 4\omega$, and thin dotted curve is for $k = 5\omega$.

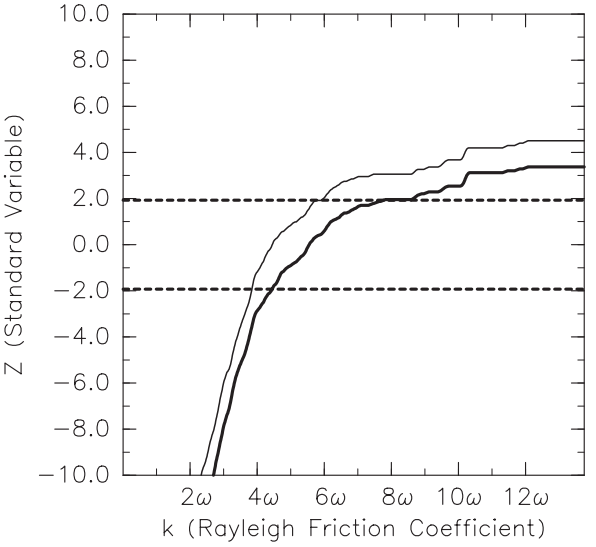

Fig. 11. Standard variable Z of the Central Limit Theorem estimated using AMeDAS data as a function of the Rayleigh friction coefficient k, normalized by ω. Solid curve shows Z for stations located at altitudes below 200 m, while the thin curve represents stations located at altitudes below 50 m. Dashed lines represent the 95% confidence limits (at ±1.96) for the standard normal distribution. See text and Appendix for details.

tributions of the surface-wind vector as a function of latitude. The authors concluded that $k \sim\omega$ ($\sim f$ in midlatitudes) would be realistic. Their theory is revisited here. We follow their method and recalculate the theoretical frequency distribution with various k values. It should be noted that as k becomes larger, the Coriolis force becomes less important in the momentum equation, and the anticlockwise frequency approaches 0.5. We assume $A = B$ for every station, and assume a constant probability distribution for the phase difference θ in Eq. (10). The latter assumption means that all θ ($-\pi/2 < \theta < \pi/2$) occur with equal frequency.

The theoretical ratios for different k are shown in Fig. 10. It should be noted that the curves in Fig. 10 shift downward if $A \neq B$ or if θ is not distributed equally but concentrated around zero (Alpert et al. 1984), as will be shown in Figs. 12a and 12b. Thus, the curves shown in Fig. 10 represent the upper limit of the ratio of anticlockwise hodographs to the total number of hodographs. Our observations undertaken at 30–46°N showed that the ratio is 0.39 (0.36) for stations located at altitudes below 200 m (50 m) (Section 3.1). Therefore, k is expected to be greater than 2ω.

4.1.b *Estimation of k based on the frequency of rotation direction of the pressure gradient force.*

We now estimate the magnitude of k in a more quantitative manner, using a method based on the assumption that when compiling a large number of samples, the frequencies of clockwise and anticlockwise rotations of the pressure gradient force would be equal. This approach can be thought of as the toss of a coin, where the probability of heads and tails is 0.5 in each case. We calculate the frequencies of clockwise and anticlockwise pressure gradient forces from the observation data and estimate the range of k based on the above assumption. Further details of this method are provided in the Appendix.

Figure 11 shows the standard variable Z defined in Eq. (A2) for stations below 200/50 m altitude as a function of k, which is normalized by ω. Two dashed lines ($Z = \pm 1.96$) represent the upper and lower confidence limits for the standard normal distribution. This figure shows that the above assumption is valid when $4\omega < k < 8\omega$ for station altitudes of < 200 m, and when $3.5\omega < k < 6\omega$ for station altitudes of < 50 m.

We analyzed a much larger number of stations than that considered in previous studies, and

utilized two different methods in estimating the magnitude of the Rayleigh friction coefficient k. We found that $k \sim \omega$ assumed by Alpert et al. (1984) may be too small; $k \sim 6\omega$ may be more appropriate, at least for plains in Japan. Thus, in the equations of motion, the pressure gradient force is primarily balanced with the frictional force, not the Coriolis force. When the pressure gradient force rotates clockwise (anticlockwise), the surface wind vector also rotates clockwise (anticlockwise). In other words, in the case of plains in Japan, the distribution of rotation direction is mainly determined by two lagged local circulations of contrasting orientations: land–sea and mountain–valley breezes. However, it should be noted that the Coriolis force has a small but non-negligible effect on the rotation direction, particularly near the coast and perhaps even over the ocean (Gille et al. 2005).

4.2 Origin of the semidiurnal component in the rotation rate

The rotation rate of the observed hodographs is well represented by the diurnal and semidiurnal components (Figs. 2, 4, 7, and 8). Here, we investigate the origin of the semidiurnal component. The semidiurnal component of surface wind detected by spectral analysis in the present study (e.g., Fig. 3) has previously been reported in other regions of the world (Kai 1984; Fujitani 1985; Orlic et al. 1988; Cokelet 1992). Cokelet (1992) suggested that the semidiurnal spectral peak should be attributed to the day–night asymmetry in solar-driven thermal forcing. Here, we seek to confirm his theory quantitatively and analytically in terms of the rotation rates of the hodographs.

We now consider the semidiurnal component of the hat-like pressure gradient force in the linearized equations of motion. Based on Eqs. (11) and (12), the horizontal momentum equations become

$$\frac{\partial u}{\partial t} - fv + ku = -F_1(t), \tag{15}$$

$$\frac{\partial v}{\partial t} + fu + kv = -F_2(t). \tag{16}$$

Equations (15) and (16) can be analytically solved for $U = \mathrm{u} + iv$, where $i = \sqrt{-1}$:

$$\begin{aligned} U = &-\frac{1}{\pi}\frac{A+iB}{if+k} \\ &-\frac{A}{2}\frac{\omega\sin(\omega t-\alpha)+(if+k)\cos(\omega t-\alpha)}{\omega^2+(if+k)^2} \\ &-i\frac{B}{2}\frac{\omega\sin(\omega t-\alpha-\theta)+(if+k)\cos(\omega t-\alpha-\theta)}{\omega^2+(if+k)^2} \\ &-\frac{2A}{3\pi}\frac{2\omega\sin 2(\omega t-\alpha)+(if+k)\cos 2(\omega t-\alpha)}{4\omega^2+(if+k)^2} \\ &-i\frac{2B}{3\pi}\frac{2\omega\sin 2(\omega t-\alpha-\theta)+(if+k)\cos 2(\omega t-\alpha-\theta)}{4\omega^2+(if+k)^2} \\ &+Ke^{-(if+k)t}, \end{aligned} \tag{17}$$

where K is a constant. In the present case, K equals zero because U diminishes to zero when the pressure gradient forces are zero. The first (constant) term and the second and third (diurnal) terms in Eq. (17) are the same as the solution by Kusuda and Alpert (1983). The fourth and fifth (semidiurnal) terms in Eq. (17) are the linear responses to the semidiurnal component of the pressure gradient forces. In the following, we estimate the parameters in Eq. (17) (i.e., α, θ, and the ratio of the amplitudes ($|A/B|$ or $|B/A|$)) based on AMeDAS observations. We then construct a modeled hodograph and compare it with the observed hodographs (Fig. 8). Note that we consider the second to fifth terms in Eq. (17) because the first term is included in the 24-hour mean wind vector. For simplicity, the parameters are estimated using only the diurnal component of the wind vector (u, v) at those stations located at altitudes below 200 m. Because (u, v) is expressed by sinusoidal functions, the diurnal component of the pressure gradient forces (i.e., α, θ, and A/B or B/A) are obtained diagnostically using Eqs. (13) and (14). Here we assumed $k = 6\omega$, following the discussion in Section 4.1. Figure 12 shows the frequency distribution of α, θ, and A/B or B/A. The phase shift α is concentrated around $-7\pi/8$ (i.e., 14 JST). The phase difference θ has a peak around zero, but the frequencies around zero are small for stations whose rotation direction is statistically significant (not shown). When θ is non-zero, the hodograph of the pressure-gradient-force vector becomes an ellipse; in other words, the system is controlled by lagged land–sea and mountain–valley breezes. When θ is exactly zero, on the other hand, the hodograph shrinks to a line. Finally, the ratio of A to B, which is related to the direction of the major axis of the hodograph, is found to be distributed

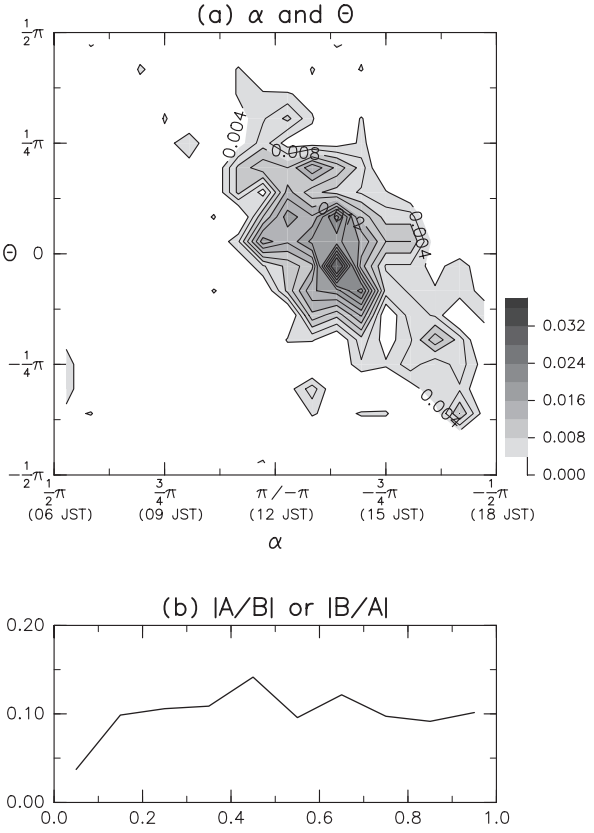

Fig. 12. Frequency distributions of (a) the phase shift α and the phase difference θ, and (b) the absolute value of the ratio between A and B, for AMeDAS stations located at altitudes below 200 m (699 stations in total). The parameters α, θ, A, and B are defined in Eqs. (7) and (8). For the ratio $|B/A|$, ($|A/B|$) is calculated when $|A|$($|B|$) is greater than $|B|$ ($|A|$).

almost equally over the range between −1 and 1. This finding suggests that the orientations of the coastlines that control the major axes of the hodographs are equally distributed around all points of the compass.

We construct a modeled hodograph based on the frequency distributions shown in Fig. 12. The frequencies of α and θ are used as they are. For simplicity, the ratios of the amplitudes, A/B or B/A, are assumed to be distributed equally within the range from −1 to 1. We also take $k = 6\omega$ and f for the value at 35°N.

Employing Eq. (17) and the parameters estimated above, we obtain a modeled rotation rate for the hodograph. Note that the semidiurnal component of the pressure gradient forces is taken into account at this stage. Figure 8 shows the time series of the modeled displacement-vector magnitude. The modeled rotation rate shows a brief stagnation during the mid-afternoon and a longer stagnation during the nighttime. The model reproduces the observed characteristics reasonably well. The modeled ratio of the semidiurnal to diurnal amplitudes is 0.42, consistent with observations (Table 1). Therefore, we conclude that the semidiurnal component of the surface wind is generated by the semidiurnal component of the hat-like pressure gradient forces.

5. Concluding remarks

We studied diurnal variations in surface wind in Japan during the period June–July–August of 1992–2006 using AMeDAS data for all of Japan (~920 stations) and MULTI data for part of Hokkaido, northern Japan (52 stations). The number of stations considered in this study is two orders of magnitude greater than that considered in previous studies, enabling us to obtain statistically significant characteristics of the wind patterns. We focused on the rotation direction and rotation rate of the surface-wind hodograph.

The rotation direction (i.e., clockwise or anticlockwise) is determined from the diurnal component extracted via harmonic analysis and rotary spectral analysis. Our analysis of six major plains within Japan reveals that clockwise (anticlockwise) hodographs are distributed in regions for which the nearest mountains are located to the right (left) when facing the sea. This finding suggests that the rotation direction is mainly determined by two lagged pressure-gradient forces of contrasting orientations: one between the land and sea and another between the plain and adjacent mountains. However, we also found that the ratio of anticlockwise hodographs to total hodographs is 0.36–0.39, significantly smaller than 0.5, suggesting a small but non-negligible contribution by the Coriolis force. Analysis of the linearized equations of motion suggests that the frictional force is ~6 times greater than the Coriolis force. In obtaining this estimation, we used the frequency distribution of the rotation direction of surface-wind vectors and the frequency distribution of the rotation direction of the pressure gradient force. At least in the case of plains in Japan, the contribution of the Coriolis force is much smaller than that assumed in previ-

ous studies; however, it still influences diurnal variations in the surface-wind system.

In characterizing the rotation rate, we found it appropriate to use the magnitude of the displacement vector (but not the angle) between consecutive hourly wind vectors. The observed rotation rate shows a brief stagnation during the mid-afternoon and a longer stagnation during the nighttime. This irregular rotation rate arises from the semidiurnal component of the wind. Based on the linearized equations of motion, we found that this semidiurnal component is caused by the semidiurnal component of the pressure gradient force, which is generated by the non-sinusoidal solar heating that occurs over the course of a day. We note that in this surface-wind system, the wind vector basically follows the pressure gradient force, as the pressure gradient force is largely balanced by the frictional force. In terms of the statistical characteristics of the hodograph, it is not necessary to consider nonlinear (advective) terms in explaining the complex rotation rate.

Our results indicate that distinct distributions of clockwise and anticlockwise hodographs should be observed upon plains with horizontal scales of 50–100 km; the distribution is easily predicted from the topography. This relationship may provide a basis for rough estimates of the transport of pollutants and heat across large plains. In addition, the boundary between areas of clockwise and anticlockwise hodographs is marked by a region with a strong diurnal variation in divergence/convergence (Mass 1982). Thus, the distribution of hodographs may provide a key to understanding local-scale convection and precipitation.

Acknowledgements

Data from the Sapporo City Multisensor were provided by the Sapporo Information Network. AMeDAS data were provided by the Japan Meteorological Agency (JMA). Topographic data were provided by the International Steering Committee for Global Mapping (http://www.iscgm.org/). This work was supported in part by the Hokkaido University Genki Project and the JGC-S Scholarship Foundation. We wish to express our gratitude to Shoshiro Minobe for useful advice regarding significance tests in spectral analysis. We also wish to thank Takenobu Toyota, Makoto Kusuda, and two anonymous reviewers for their helpful comments. The figures were drawn using the GFD-DENNOU Library.

Appendix

Estimation of k based on the frequency of rotation direction of the pressure gradient force

The assumption here is that when collecting a large number of samples, the frequencies of clockwise and anticlockwise rotations of the pressure-gradient-force vector should each be 0.5. Let the clockwise and anticlockwise rotations be expressed by $X_j = 1$ and 0, respectively, where j denotes each station. The number of stations with a clockwise force vector, out of n stations in total, S_n, is

$$S_n = X_1 + X_2 + \cdots + X_n. \tag{A1}$$

S_n is known to follow a binomial distribution. According to the Central Limit Theorem, the standard variable Z, defined as

$$Z = \frac{S_n - np}{\sqrt{np(1-p)}}, \tag{A2}$$

where p is the probability of each event ($p = 0.5$ in the present case), follows the standard normal distribution $N(0,1)$. Once S_n is determined from the observation data, we can determine the range of k values for which the assumption is significant at the 95% confidence interval by finding k for $Z = \pm 1.96$ (e.g., Wilks 2006, Chapter 5).

The procedure employed in determining $S_n(k)$ is as follows. When k is specified, the pressure gradient forces can be estimated diagnostically using Eqs. (13) and (14), with the wind components described by sinusoidal functions. Here, we assume that the pressure-gradient-force vector can be approximated solely in terms of the diurnal harmonic component. The rotation direction of the pressure-gradient-force vector is then obtained for each station. Finally, $S_n(k)$ is calculated for each k. For example, for stations located at altitudes below 200 m ($n = 699$), when $k = 3.0 \times 10^{-4} \cong 4\omega$ ($4.0 \times 10^{-4} \cong 5.5\omega$), $S_n(k) = 318$ (348) and $Z = -2.4$ (0.11). This means that $k \cong 5.5\omega$ is statistically significant within a 95% confidence interval, but $k \cong 4\omega$ is not.

References

Alpert, P., M. Kusuda, and N. Abe, 1984: Anticlockwise rotation, eccentricity and tilt angle of the wind hodograph. Part II: An observational study. *J. Atmos. Sci.*, **41**, 3568–3583.

Barnes, S.L., 1964: A technique for maximizing details in numerical weather map analysis. *J. Appl. Me-*

teor., **3**, 396–409.
Bastin, S., P. Drobinski, A. Dabas, P. Delville, O. Reitebuch, and C. Werner, 2005: Impact of the Rhone and Durance valleys on sea-breeze circulation in the Marseille area. *Atmos. Res.*, **74**, 303–328.
Cokelet, E.D., 1992: Axial and cross-axial winter winds over Puget Sound. *Mon. Wea. Rev.*, **120**, 826–834.
Fisher, E.L., 1960: An observational study of the sea breeze. *J. Meteor.*, **17**, 645–660.
Fujitani, T., 1985: Characteristics of the diurnal variation and spectrum of wind speed in the atmospheric boundary layer at the Tsukuba Science City. *Tenki*, **32**, 259–269 (in Japanese).
Furberg, M., D.G. Steyn, and M. Baldi, 2002: The climatology of sea breezes on Sardinia. *Intl. J. Climatol.*, **22**, 917–932.
Gille, S.T., S.G. Llewellyn Smith, and N.M. Statom, 2005: Global observations of the land breeze. *Geophys. Res. Lett.*, **32**, L05605, doi:10.1029/2004GL022139.
Gonella, J., 1972: A rotary-component method for analysing meteorological and oceanographic vector time series. *Deep-Sea Res.*, **19**, 833–846.
Haurwitz, B., 1947: Comments on the sea-breeze circulation. *J. Meteor.*, **4**, 1–8.
Helmis, C.G., K.H. Papadopoulos, J.A. Kalogiros, A.T. Soilemes, and D.N. Asimakopoulos, 1995: Influence of background flow on evolution of Saronic Gulf sea breeze. *Atmos. Environ.*, **29**, 3689–3701.
Itoh, H. and T. Kawasoe, 1983: Land and sea breezes in Wakayama prefecture. *Tenki*, **30**, 151–159 (in Japanese).
Itoh, H. and A. Noda, 1989: Seasonal changes in the rotational direction indicated in hodographs of diurnal wind variation. *Tenki*, **36**, 305–317 (in Japanese).
Kai, K., 1984: Power spectra of long-period fluctuations of horizontal wind speed and atmospheric pressure measured at the 30-m meteorological tower. *Tenki*, **31**, 235–241 (in Japanese).
Kondo, H., 1990: A numerical experiment of the "extended sea breeze" over the Kanto Plain. *J. Meteor. Soc. Japan*, **68**, 419–434.
Krishnamurti, T.N. and L. Bounoua, 1996: *An introduction to numerical weather prediction techniques*. CRC Press, 293 pp.
Kurita, H., H. Ueda, and S. Mitsumoto, 1990: Combination of local wind systems under light gradient wind conditions and its contribution to the long-range transport of air pollutants. *J. Appl. Meteor.*, **29**, 331–348.
Kusuda, M. and P. Alpert, 1983: Anti-clockwise rotation of the wind hodograph. Part I: Theoretical study. *J. Atmos. Sci.*, **40**, 487–499.
Kusuda, M. and N. Abe, 1989: The contribution of horizontal advection to the diurnal variation of the wind direction of land-sea breezes: Theory and observations. *J. Meteor. Soc. Japan*, **67**, 177–185.
Lecluyse, A. and J. Neumann, 1986: On the local rate of turning of wind direction. *Quart. J. Roy. Meteor. Soc.*, **112**, 285–288.
Mass, C., 1982: The topographically forced diurnal circulations of western Washington State and their influence on precipitation. *Mon. Wea. Rev.*, **110**, 170–183.
Miller, S.T.K., B.D. Keim, R.W. Talbot, and H. Mao, 2003: Sea breeze: Structure, forecasting, and impacts. *Rev. Geophys.*, **41(3)**, 1011, doi:10.1029/2003RG000124.
Mori, Y., 1982: On climatological aspects of daily variation of surface wind in Japan. *Tenki*, **29**, 223–230 (in Japanese).
Neumann, J., 1977: On the rotation rate of the direction of sea and land breezes. *J. Atmos. Sci.*, **34**, 1913–1917.
Nitis, T., D. Kitsiou, Z.B. Klaic, M.T. Prtenjak, and N. Moussiopoulos, 2005: The effects of basic flow and topography on the development of the sea breeze over a complex coastal environment. *Quart. J. Roy. Meteor. Soc.*, **131**, 305–327.
Ookouchi, Y. and Y. Wakata, 1984: Numerical simulation for the topographical effect on the sea-land breeze in the Kyushu island. *J. Meteor. Soc. Japan*, **62**, 864–879.
Orlic, M., B. Penzar, and I. Penzar, 1988: Adriatic sea and land breezes: Clockwise versus anticlockwise rotation. *J. Appl. Meteor.*, **27**, 675–679.
Prezerakos, N.G., 1986: Characteristics of the sea breeze in Attica, Greece. *Bound.-Layer Meteor.*, **36**, 245–266.
Puygrenier, V., F. Lohou, B. Campistron, F. Said, G. Pigeon, B. Benech, and D. Serca, 2005: Investigation on the fine structure of sea-breeze during ESCOMPTE experiment. *Atmos. Res.*, **74**, 329–353.
Simpson, J.E., 1996: Diurnal changes in sea-breeze direction. *J. Appl. Meteor.*, **35**, 1166–1169.
Staley, D.O., 1957: The low-level sea breeze of northwest Washington. *J. Meteor.*, **14**, 458–470.
Steyn, D.G. and G. Kallos, 1992: A study of the dynamics of hodograph rotation in the sea breezes of Attica, Greece. *Bound.-Layer Meteor.*, **58**, 215–228.
Wilks, D.S., 2006: *Statistical methods in the atmospheric sciences*., Academic Press, 627 pp.
Zhong, S. and E.S. Takle, 1992: An observational study of sea- and land-breeze circulation in an area of complex coastal heating. *J. Appl. Meteor.*, **31**, 1426–1438.
Zhong, S. and E.S. Takle, 1993: The effects of large-scale winds on the sea-land-breeze circulations in an area of complex coastal heating. *J. Appl. Meteor.*, **32**, 1181–1195.